ROYAL SOCIETY
OF CHEMISTRY

PAPER

Check for updates

Designing inorganic–magnetic–organic nanohybrids for producing effective photocatalysts for the purification of water

Osama Saber, [ID] *[ab] Mostafa Osama,[a] Adil Alshoaibi,[a] Nagih M. Shaalan[ac] and Doaa Osama[a]

The present study describes a new strategy for modifying the structure of zinc oxide for removing colored pollutants from water after a few minutes of light irradiation. In this context, the magnetic nanocomposite was combined with the nanolayers of Al/Zn to build inorganic–magnetic nanohybrids. The long chains of hydrocarbons of stearic acid have been used as pillars to widen interlayered spacing among the nanolayers to build organic–magnetic–inorganic nanohybrids. These nanohybrids were used as sources for designing zinc oxide nanohybrids to purify water from the green dyes using UV-light. The optical measurements showed that the nanohybrid structure of zinc oxide led to a clear reduction in the band gap energy from 3.30 eV to 2.75 eV to be more effective. In addition, a complete removal of naphthol green B was achieved after 15 min in the presence of zinc oxide nanohybrid using UV-light. The kinetic study showed that the reaction rate for the photocatalytic degradation of the pollutants was faster than that of the conventional photocatalysts. Finally, this strategy for designing photoactive nanohybrids led to positive results for overcoming environment- and water-related problems using the fast technique for purifying water.

Introduction

In recent years, environment- and water-related problems have become great challenges for the scientific community.[1,2] These international challenges are due to the rapidly growing population and industries, which has led to increasing and worsening environmental problems linked to water. Most organic dyes such as textile dyes and surfactants are not easily biodegradable. Therefore, they belong to the category of colored hazardous pollutants. Photocatalytic degradation is a benign solution for purifying water from organic dyes using photocatalysts and light.[3–5] Semiconductor photocatalysts are very familiar in this area to solve environmental problems and purify wastewater.[6–9]

According to the basic principle of heterogeneous photocatalysis, the electronic structure of a semiconductor has a strong effect on the performance of photocatalytic degradation of pollutants.[10,11] Depending on the band gap (E_g) of the semiconductor, the electrons, which exist in the valence band (VB) of the photocatalyst, are excited and transferred to the empty conduction band (CB) by absorbing light to create

electron–hole pairs. However, they start to recombine within a few nanoseconds if the photogenerated charge carriers are not utilized in photocatalytic reactions. Also, the wide band gap energy of semiconductors is hindered by the poor absorption of light. In addition, the poor selective adsorption and high concentration of organic pollutants in industrial waste water causes the poisoning of photocatalysts and decreases their activity in the water treatment process.[10,11]

For example, titanium oxide, which is one of the most famous photocatalysts in this field, has limited applications.[12–14] However, zinc oxide, which was suggested to be an alternative photocatalyst to titanium oxide,[15,16] has shown low performance for photocatalytic degradation in many studies because of the high rate of recombination reactions between the photogenerated electrons and the holes of zinc oxide.[17–19] These disadvantages obstruct the commercialization of photocatalytic decomposition processes; thus, overcoming these drawbacks is the main challenge in the design of photocatalysts.

Recently, several researchers have designed heterostructures and hybrid materials for overcoming this challenge. Multivariate metal–organic frameworks (MTV-MOFs) have recently emerged as an exciting class of crystalline materials with broad visible-light absorption for environmental remediation.[20] An excellent photocatalytic degradation performance of the pollutants was observed by nitrogen-doped carbon-based nanocomposites (ZnO/Ag$_2$O–C), which achieved degradation of approximately 90.7% of the pollutants within 60 min with

[a]Department of Physics, College of Science, King Faisal University, P. O. Box 400, Al-Ahsa 31982, Saudi Arabia

[b]Egyptian Petroleum Research Institute, P. O. Box 11727, Nasr City, Cairo, Egypt

[c]Physics Department, Faculty of Science, Assiut University, Assiut 71516, Egypt. E-mail: osmohamed@kfu.edu.sa; Tel: +20-013-5899440

a rate constant of 0.0083 min^{-1}.[21] A ternary PSCN/Ag/AgI/WO$_3$ heterostructure was prepared and used for the photocatalytic removal of toxic malachite green dye from wastewater, indicating excellent photoactivities in the visible light region.[22] In the same trend, a ternary composite (Ag$_2$CO$_3$/BiOBr/CdS) was fabricated and used as a photocatalyst for the removal of antibiotic drug pollutants from wastewater, giving 98.79% removal of tetracycline with 70 min of light irradiation.[23]

To increase the recycling of photocatalysts, a new generation of photocatalysts has emerged depending on the combination between photocatalysts and magnetic materials. Shekofteh-Gohari *et al.*[24] introduced a helpful insight into the preparation of magnetically separable photocatalysts based on ZnO and their applications for the degradation of different pollutants.

Several techniques have used for modifying the structure of zinc oxide to solve its problems by narrowing its band gap energy to make it more active and increase the absorbed quantum yield from light. The formation of nanostructures,[25] combination with carbon nanorods and nanotubes,[26] and introducing surface defects were used as good solutions for improving the activity of zinc oxides. Also, for preventing the disadvantages of zinc oxide, doping processes with transition elements, in addition to morphological changes,[27] were studied as suitable solutions for increasing the performance of zinc oxide for the photocatalytic degradation of pollutants. In this context, the optical properties and activity of zinc oxide were developed through morphological changes from nanoparticles[28] to nanorods.[29] In addition, the zinc oxides nanotubes[30] and nanowires[31] were suggested to be active photocatalysts.[32]

Many researchers have used transition elements for doping zinc oxide to make effective photocatalysts.[33–37] The insertion of sulfur inside the structure of ZnO improved the charge separation by preventing the recombination process between electrons and holes.[38] The results of the study by Adeel *et al.* showed high photocatalytic degradation of rhodamine blue and methylene blue under UV irradiation using ZnO films, which were modified by the addition of Ag and Al.[39] The introduction of nitrogen using micro-emulsion method increased the optical properties and activity of ZnO nanospheres.[40] In addition, several studies have concluded that the addition of aluminum and iron as dopants inside ZnO structures converted their transparent thin films to make them useful for photocatalytic applications and solar cells.[41–46] This positive effect of the addition of aluminum inside zinc oxide was confirmed by our previous research.[9] Thus, the current research aims to improve the photocatalytic activity of the ZnO structure by building nanohybrids based on organic, magnetic, and inorganic species by an unconventional technique. In conventional methods,[47] multi-steps were used for mixing one or two elements for zinc oxides. However, it is difficult to obtain a homogenous distribution for all dopants in the matrix of ZnO in this way.

Following this trend, the current study has used organic and magnetic species to reduce the band gap energy of zinc oxide to make it effective for purifying water from colored pollutants. In this study, series of zinc oxides based on magnetic, inorganic, and organic species were prepared by building inorganic–magnetic–organic and inorganic–magnetic nanohybrids. The inorganic–magnetic–organic nanohybrids were formed by the intercalation reactions of long chains of hydrocarbons of stearic acids with the insertion of magnetic nanoparticles of cobalt iron oxide nanocomposites inside the nanolayered structures of zinc and aluminum. Organic species are used as pillars to widen the interlayered spacing of the nanolayered structures to allow for the insertion of magnetic nanoparticles between the nanolayers of zinc and aluminum. Also, inorganic–magnetic nanohybrids were prepared without long chains of organic acid to identify the role and effect of organic species. These nanohybrids were used for producing zinc oxide nanohybrids. Zinc oxide nanohybrids were tested for purifying water through the photocatalytic degradation of the colored pollutants. At the same time, the optical properties and activity of the nanohybrids were studied and compared with those of conventional photocatalysts. Also, kinetic study has carried out for evaluating the activity of the prepared nanohybrids.

Results

Characterization of the prepared filler

Very fine nanoparticles of cobalt iron oxide nanocomposite were prepared and characterized for use as a filler and insertion among the nanolayers of the nanolayered structures. In this context, X-ray diffraction was used for confirming the structure of the prepared cobalt iron oxide nanocomposite. Fig. 1a showed the X-ray diffraction pattern of the prepared cobalt iron oxide nanocomposite.

The X-ray diffraction pattern showed weak peaks at $2\Theta = 35.56°$, $41.6°$, $57.28°$, and $62.9°$, agreeing with the *d*-spacings at 0.25 nm, 0.21 nm, 0.16 nm, and 0.15 nm, respectively. By comparing with the standard diffraction pattern of JCPDS 79-1744, Fig. 1a revealed that the prepared cobalt iron oxides have a CoFe$_2$O$_4$ structure. Transmission electron microscopy was used for measuring the nanosize of the particles of the prepared cobalt iron oxides. Fig. 1b showed strong aggregates of nanoparticles because of the magnetic behavior of cobalt iron oxides. By magnification, very fine nanoparticles were observed in Fig. 1c. More magnification showed that the size of the particles of the prepared cobalt iron oxides is less than 5 nm, as seen in Fig. 1c (inset).

Design of organic–inorganic–magnetic nanohybrids

Organic–inorganic–magnetic nanohybrids appear to be very versatile because they can produce an unlimited set of known or unknown properties. In this way, nanohybrids were designed by combination between one dimensional nanoparticles of magnetic nanocomposites and two dimensional nanolayered structures in addition to long chains of organic acid. This combination was achieved in an ordered arrangement by building Al/Zn nanolayered structures, which have cationic nanolayers. In the presence of stearic acid (CH$_3$(CH$_2$)$_{16}$COO$^-$), the long chains of the aliphatic acid were intercalated among the nanolayers for neutralizing their positive charges. At the same time, the long chains of stearate anions worked as pillars
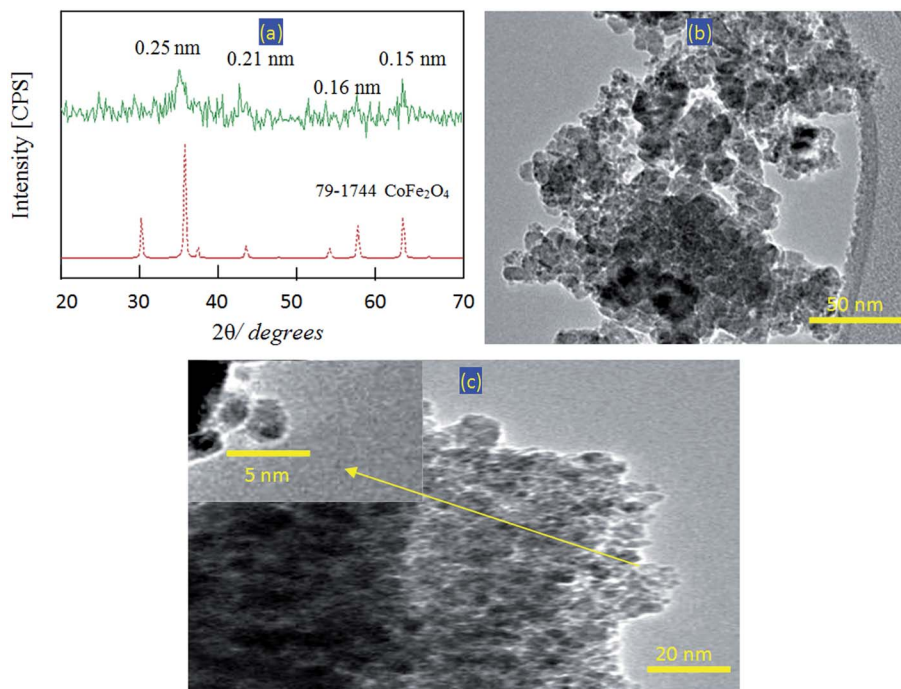
Fig. 1 The prepared cobalt iron oxides nanocomposite: (a) X-ray diffraction pattern, (b) TEM image at 50 nm, and (c) TEM image at 20 nm (inset at 5 nm).

for building the nanolayered structures. In addition, these pillars expanded and widened the interlayered spacing among the nanolayers to produce enough space for existing cobalt iron oxide magnetic nanoparticles. To indicate the positive role of organic species in designing this nanohybrid, pure Al/Zn with a nanolayered structure was prepared for comparison. Also, the Al/Zn nanolayered structure was modified by the nanoparticles of cobalt iron oxide nanocomposites without organic species to study the inorganic–magnetic nanohybrid. The X-ray diffraction patterns of the prepared nanolayered structures and nano-hybrids are displayed in Fig. 2.

Fig. 2a shows the X-ray diffraction pattern of the pure Al/Zn nanolayered structure ZAO. Sharp and symmetric peaks were observed at $2\Theta = 11.62°, 23.36°,$ and $34.54°$ corresponding to the d-spacing of 0.76 nm, 0.38 nm, and 0.26 nm, respectively. These peaks are due to the reflections of the main planes of [003], [006], and [009]. The clear arrangement between these reflections (0.76 nm = 2 × 0.38 nm = 3 × 0.26 nm) confirmed the formation of the nanolayered structures of the natural hydrotalcite (JCPDS file no. 37-629) and zinc aluminum carbonate hydroxide hydrate (JCPDS file no. 38-486). The other reflections of the planes [012], [015], [110], and [113] of the nanolayered structures of the natural hydrotalcite were observed at $2\Theta = 39.16°, 46.56°, 60.05°,$ and $61.44°$, matching with the d-spacing of 0.23 nm, 0.19 nm, 0.17 nm, 0.153 nm, and 0.150 nm, respectively. The crystal parameters (a, c) could be calculated depending on the d-spacing of the planes [003] and [110], respectively. The first parameter was $2 × d_{[110]} =$ 0.306 nm. It means that the average distance between Zn-cation and Al-cation is 0.306 nm, agreeing with the previous published data of zinc aluminum carbonate hydroxide hydrate (JCPDS file

no. 38-486). The second parameter was assessed by $3 × d_{[003]} =$ 2.28 nm. It was similar to that reported for the natural hydrotalcite.
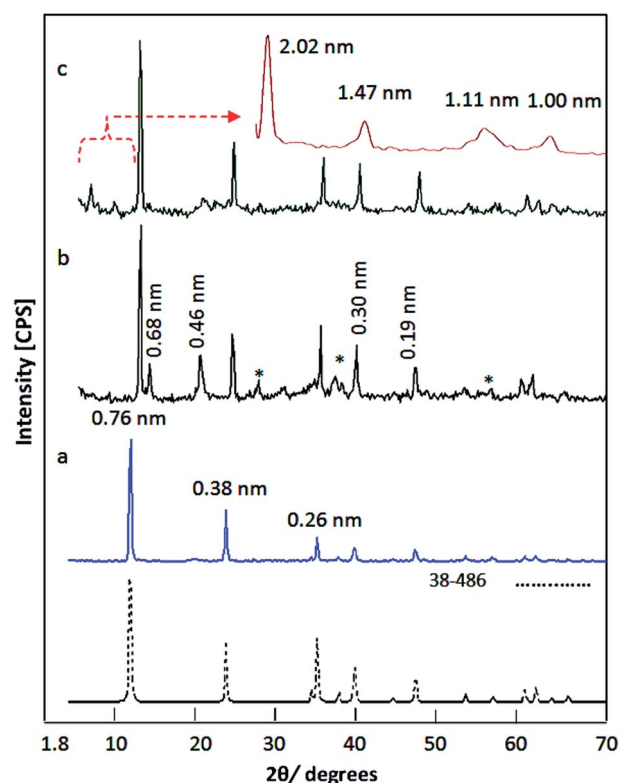

Fig. 2 X-ray diffraction patterns of (a) ZAO, (b) ZH-1, and (c) ZH-2.

By incorporating the nanoparticles of cobalt iron oxide nanocomposite with the pure Al/Zn nanolayered structures without organic species, ZH-1 was formed to build the inorganic–magnetic nanohybrid. Fig. 2b showed a little shift from the main peaks of the nanolayered structures in addition to the new emerging peaks after building the nanohybrid ZH-1. The crystal parameter (a), which depends on the reflection of the plane [110], did not change. At the same time, a little change was observed for the parameter (c) from 2.280 nm to 2.265 nm. It means that the nanohybrid ZH-1 has the same nanolayered structure with new phases. The appearance of clear peaks at 2Θ = 13.01°, 19.48°, and 26.78° for d-spacing of 0.68 nm, 0.455 nm, and 0.331 nm, respectively, indicated the growth of new phase hydrozincite $Zn_5(OH)_6(CO_3)_2$. In addition, the presence of magnetic nanoparticles was confirmed by observing the characteristic peaks of cobalt iron oxides, which was marked with (*) in Fig. 2b. It means that the magnetic nanoparticles were supported on the external surface of the nanolayered structure of Al/Zn because the small interlayered spacing between the nanolayers is unsuitable for inserting the nanoparticles because of their size. Also, the XRD results showed their peaks, indicating that these nanoparticles are not covered or coated by the nanolayers.

By intercalating the long chains of stearic acid (CH_3(CH_2)$_{16}COO^-$) with the Al/Zn nanolayered structures in the presence of nanoparticles of cobalt iron oxides, organic–inorganic–magnetic nanohybrid ZH-2 was formed through host–guest interaction. The X-ray diffraction pattern of ZH-2, which is displayed in Fig. 2c, showed new peaks at low 2theta in addition to the original peaks of the nanolayered structures. In the same time, the peaks of the nanoparticles of magnetic nanocomposite became unclear. The new peaks of the nanohybrid ZH-2 became clearer after measuring the X-ray diffraction at low range of 2theta from 4–10, as seen in Fig. 2c (inset). A sharp peak was observed at 2.02 nm, indicating that the interlayered spacing of the nanolayered structure expanded and widened from 0.755 nm to 2.02 nm. This spacing could allow for the nanoparticles of cobalt iron oxides to intercalate among the nanolayers of the nanolayered structure because the peaks of cobalt iron oxides are not clear in Fig. 2c. It means that the nanohybrid ZH-2 consists of nanolayered structures having organic species and magnetic nanoparticles. This finding was confirmed by transmission electron microscopy (TEM). The TEM images of the nanohybrid ZH-2 are displayed in Fig. 3. Fig. 3a shows that the nanohybrid ZH-2 has nanoplatelets with a size less than 50 nm. Also, very small black dotes, which are marked by an arrow, are observed in Fig. 3a, representing the magnetic nanoparticles of cobalt iron oxides. By magnification, Fig. 3c confirmed the presence of the magnetic nanoparticles. In addition, Fig. 3b confirmed the nanolayered structures with an interlayer spacing of 2 nm.

The presence of magnetic, inorganic elements, and organic species was confirmed by energy dispersive X-ray spectroscopy (EDX). Although the EDX spectra indicate the local data of different elements in the outermost layers of the platelets of the nanohybrid, the magnetic elements were identified by clear peaks for cobalt and iron, as seen in Fig. 4. Also, the inorganic

elements (zinc, aluminum, and oxygen) were observed by sharp peaks in Fig. 4. In addition, a strong peak for carbon was observed, thus confirming the presence of organic species.

Fourier transform infrared (FT-IR) spectroscopy was applied to compare the function groups of the nanohybrids ZH-1 and NH-2, as shown in Fig. 5. For the nanohybrid ZH-1, Fig. 5a showed an absorption band at 3460 cm^{-1}, indicating the stretching mode of hydroxyl groups. The large broadness of the OH band between 3500 cm^{-1} and 3400 cm^{-1} indicated the presence of two types of hydroxyl groups, which belonged to the nanolayered structures and hydrozincite phase. The shoulder that is recorded at about 3000 cm^{-1} is due to the hydrogen bonds of carbonate anions. The bands at 1495 cm^{-1} and 1364 cm^{-1} should be due to the vibrational mode of the interlayer carbonate anions. The other band at 1438 cm^{-1} represented the carbonate anions of hydrozincite phase, agreeing with XRD results. The weak band at 2202 cm^{-1} is due to the presence of cyanate anions, indicating that the nanohybrid ZH-1 has two types of interlayered anions. The bands observed below 1000 cm^{-1} could be ascribed to Zn–O and Al–O.

For the nanohybrid ZH-2, Fig. 5b confirmed the presence of long chains of organic species in the IR spectrum because the stretch absorption of carbon–hydrogen was observed by sharp peaks at 2918 cm^{-1} and 2850 cm^{-1}. Also, the bending mode of the carbon–hydrogen was clear by observing the band at 1468 cm^{-1}. The symmetric stretching vibration of carboxylate, which belonged to the aliphatic acid, was observed at 1540 cm^{-1}. Furthermore, the absorption at 1398 cm^{-1} is assigned to the asymmetric stretching vibration of carboxylate. In addition, the absorption band of the hydroxyl groups of the nanolayered structure was observed at 3467 cm^{-1}. In the same trend, the presence of long chains of organic species inside the nanohybrid ZH-2 was confirmed by thermal analyses.

Thermogravimetric and differential scanning calorimetric (TGA-DSC) curves showed that degradation occurs through a continuous process with various mass rate losses, depending on the nature of the interlayer species. The DSC curve of the nanohybrid ZH-2 showed two series of peaks, as shown in Fig. 6a. The first series is endothermic peaks at 132 °C, 150 °C, and 282 °C, which are ascribed to the removal of water and inorganic anions. The second series is exothermic peaks at 367 °C, 456 °C, and 522 °C, representing the oxidation reactions of the organic species. Also, there is a weak exothermic peak at about 210 °C, indicating the oxidation of divalent cobalt to trivalent cobalt in $CoFe_2O_4$. From the TG curve, Fig. 6b showed a large weight loss, confirming the presence of organic species. The weight loss of 18%, which happened up to 300 °C, represents the internal content of water and inorganic anions inside the nanohybrid ZH-2. In the same way, 30% weight loss, which occurred up to 700 °C, is due to the internal content of organic species inside the nanohybrid ZH-2. It means that ZH-2 is mainly an organic–inorganic–magnetic nanohybrid.

Design of nanohybrids based on oxides

The main reason for designing nanohybrids with organic and inorganic species is directed to produce stable and effective zinc
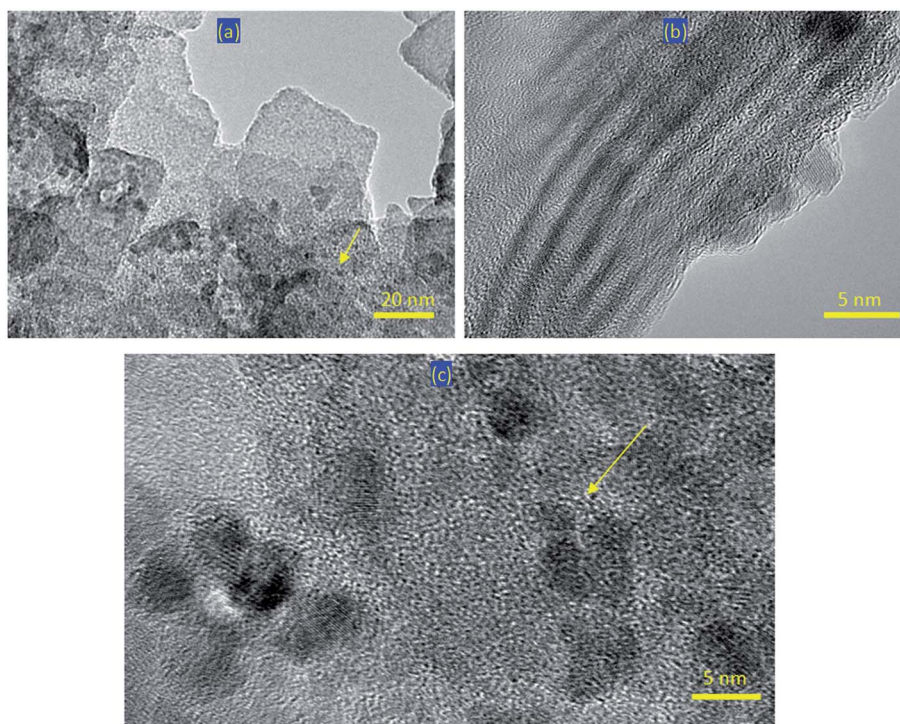
RSC Advances

Paper

Fig. 3 TEM images of the nanohybrid ZH-2: (a) the first location at 20 nm, (b) the second location at 5 nm, and (c) the first location at 5 nm.
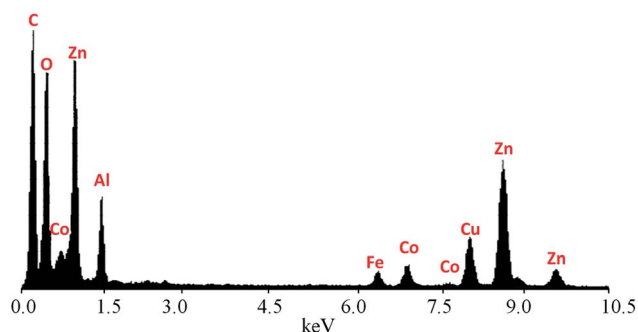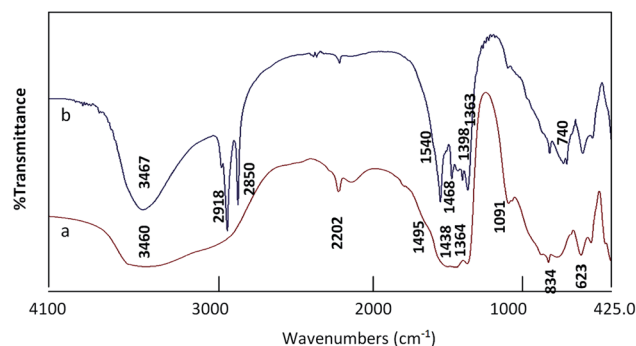

Fig. 4 EDX spectrum of the nanohybrid ZH-2.

Fig. 5 FT-IR spectra of (a) the nanohybrid ZH-1 and (b) the nanohybrid ZH-2.

oxide nanohybrids and nanocomposites with distinguished properties. Therefore, the prepared nanohybrids were thermally treated at 500 °C to remove unstable species and create new optically-active sites.

X-ray diffraction was used to identify the produced structures from the calcination of nanohybrids. Fig. 7 shows X-ray diffraction patterns of ZAO-500, ZH-1-500, and ZH-2-500. The XRD pattern of ZAO-500 exhibited new weak peaks at $2\Theta = 32.01°, 34.32°, 36.49°, 47.71°, 7.05°,$ and $62.81°$, in addition to the original peaks of the nanolayered structures that disappeared, as shown in Fig. 7a. By comparing with the diffraction lines of the zinc oxide crystal (JCPDS no. 36-1451) and the standard entire diffraction pattern of the zincite phase (JCPDS no. 75-576), ZAO-500 has a similar structure for zinc oxide. The broad and diffuse peaks of ZAO-500 indicated the nanoscale crystallinity of the ZnO particles with randomly oriented

polycrystalline because of doping with aluminum. In case of the nanohybrid ZH-1-500, the X-ray diffraction patterns showed that this structure tends to be amorphous because the peaks of zinc oxide became unclear. Only two peaks of zinc oxide, which are observed at $2\Theta = 36.30°$ and $62.92°$, were identified in the X-ray diffraction pattern of ZH-1-500. In addition, the weak peaks of cobalt iron oxides were also observed at $2\Theta = 30.29°, 35.65°, 37.78°, 40.36°, 53.77°, 57.28°,$ and $64.86°$ in Fig. 7b. It means that ZH-1-500 has two different types of structures—cobalt iron oxides and Al-doped zinc oxides. For the nanohyrid ZH-2-500, Fig. 7c shows clear and sharp peaks at 0.28 nm, 0.26 nm, and 0.24 nm, indicating the crystalline structure. Also, weak peaks were observed at 0.19 nm, 0.16 nm, 0.15 nm, and 0.14 nm. These diffraction lines agree with the peaks of the zinc oxide crystal (JCPDS no. 36-1451) and the standard entire diffraction
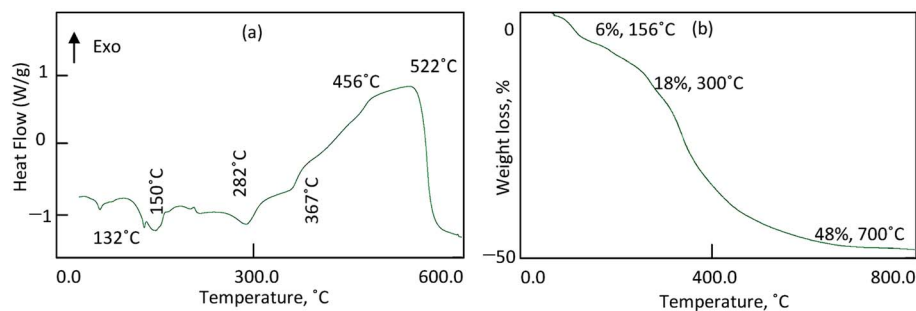
Fig. 6 Thermal analyses of the nanohybrid ZH-2: (a) differential scanning calorimetric and (b) thermal gravimetric analysis.
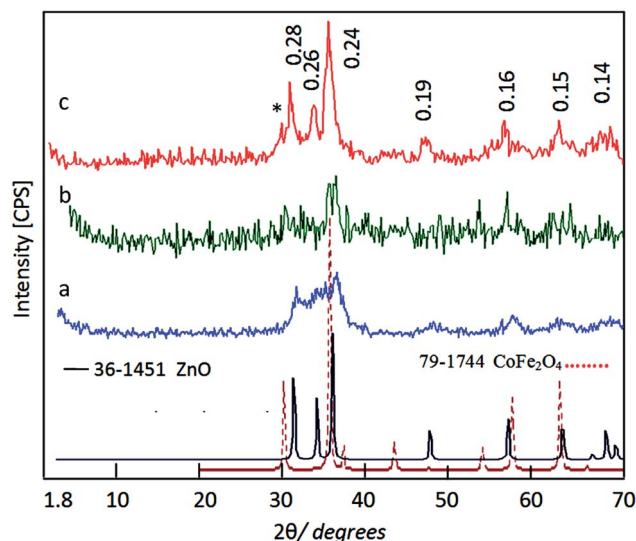

Fig. 7 X-ray diffraction patterns of (a) ZAO-500, (b) ZH-1-500, and (c) ZH-2-500.

pattern of the zincite phase (JCPDS no. 75-576). In addition, a weak peak was observed at 0.30 nm and marked with (*) in Fig. 7c. At the same time, Fig. 7c revealed that the characteristic peak of cobalt iron oxides at 0.25 nm overlapped with the peak of zinc oxide at 0.26 nm. These XRD results can conclude that ZH-2-500 has zincite phase doping with aluminum and cobalt iron oxides.

Fig. 8a showed that ZH-1-500 has two structures—white nanoparticles and large black plates—agreeing with XRD results. The chemical composition of the black plates was determined by EDX analysis. Fig. 8b showed that the black plates are zinc oxide-doped with aluminum with Zn/Al molar ratio = 3.5, agreeing with the nanolayered structure of Al/Zn LDH. It means that the other white nanoparticles are the cobalt iron oxide nanocomposite.

Fig. 8c showed one phase for ZH-2-500, as seen in the SEM image. The chemical composition of ZH-2-500, which is determined by EXD analysis, confirmed the formation of zinc oxide doped with Al, Co, and Fe, agreeing with the XRD results. Fig. 8d indicated 2.01% of Co and 1.38% of Fe inserted in the ZnO structure in addition to the presence of 10.96% of Al.

The TEM images of ZH-2-500 confirmed this finding, as shown in Fig. 9. Clear nanoparticles were observed for ZH-2-500, as seen in Fig. 9a. It indicated that the width of ZH-2-500 is 20 nm. Also, very fine white spots were observed and marked by an arrow on the surface of the nanoparticles. These spots represent the cobalt iron oxide nanocomposites. These white spots became clearer by magnification, as seen in Fig. 9b. Fig. 9b confirmed the presence of white spots and measured their sizes. It indicated that the size of cobalt iron oxides is less than 2 nm. Energy dispersive X-ray spectroscopy (EDX) analysis of ZH-2-500 confirmed the presence of magnetic elements, which showed two weak peaks for cobalt and iron (Fig. 9b (inset)). Also, the inorganic elements (zinc, aluminum, and oxygen) were observed by sharp peaks in Fig. 9b (inset).

According to the results of XRD and the images of TEM, the nanohybrids based on zinc oxide were clear from the thermal decomposition of the organic–inorganic–magnetic nanohybrid, as shown in Fig. 10. Fig. 10 shows the schematic representation for transforming the organic–inorganic–magnetic nanohybrid to zinc oxide nanohybrids. Also, Fig. 10 indicated the difference between the thermal decomposition of the organic–inorganic–magnetic nanohybrid and the inorganic–magnetic nanohybrid. The presence of the magnetic nanoparticles of cobalt iron oxides inside the nanolayered structure of Al/Zn gave a chance for the incorporation of cobalt iron oxides nanoparticles with the produced nanoparticles of the Al-doped ZnO during the thermal decomposition of organic species and the crystallization process of zinc oxide, creating new optical-active sites at ZH-2-500. In case of the inorganic–magnetic nanohybrid, the presence of the magnetic nanoparticles of cobalt iron oxides on the external surface of the nanolayered structure did not allow for the incorporation process with the produced Al-doped ZnO. Therefore, the XRD results of ZH-1-500 showed two crystalline structures for zinc oxide and cobalt iron oxides.

Optical properties

Zinc oxide is familiar for the researchers in the field of optical application as one of the most famous photoactive materials. However, its optical applications are concentrated to the UV region. Therefore, many studies have been published in the literature for developing the structure and morphology of zinc oxide to advance its optical behavior by increasing the range of its absorbance and decreasing its band gap energy.
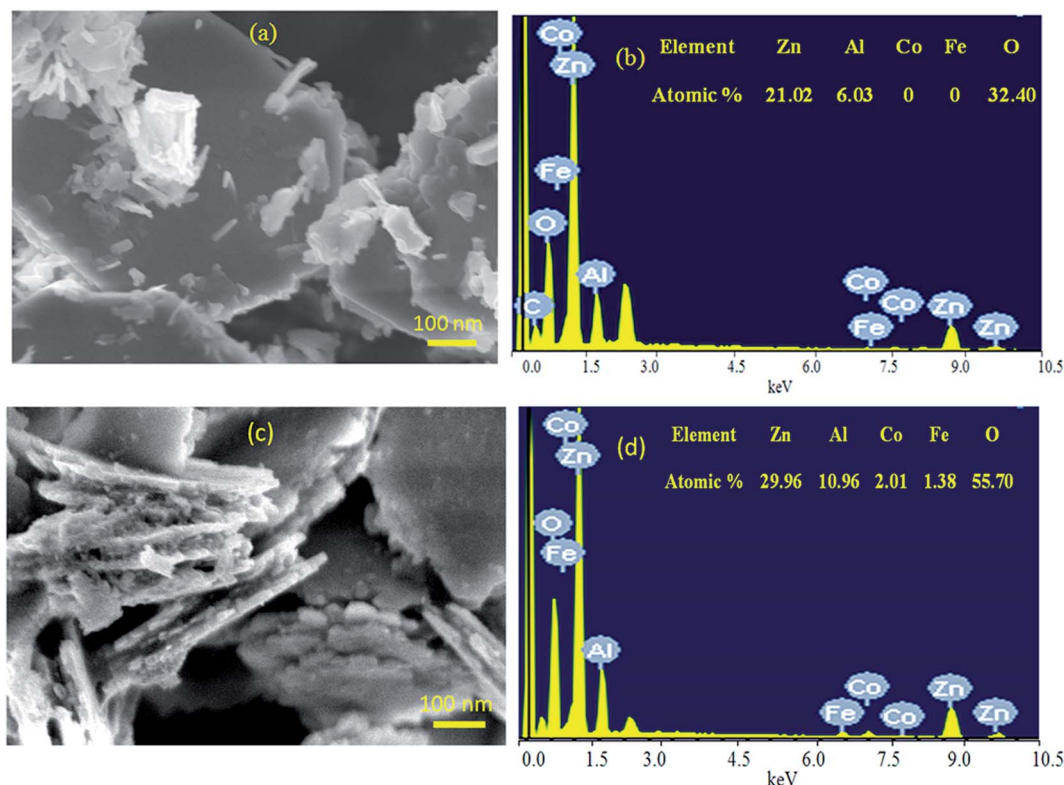
Fig. 8 ZNH-1-500: (a) SEM images, (b) EDX spectrum; ZNH-2-500: (c) SEM images, (d) EDX spectrum.

In this way, the optical absorbance and band gap energy of the prepared nanohybrids were studied and compared using the UV-Vis absorption technique, which is considered a powerful tool for providing important details about their optical properties.

Fig. 11 shows the UV-Vis absorbance of ZAO-500, ZH-1-500, and ZH-2-500. Fig. 11a indicates that ZAO-500 is active in the UV region because it has absorption in the wavelength range of 200–350 nm. At the same time, there is no absorption in the visible region above 400 nm. By modifying the structure of ZAO-500 by combining with magnetic nanocomposites, the optical properties of ZH-1-500 improved, as shown in Fig. 11b. New absorbance band was observed in the visible region at 650 nm. It means that the introduction of magnetic nanocomposites with the Al-doped zinc oxide has a positive effect on its optical properties. However, the low intensity of this new band in the visible region indicated that this positive effect is limited. This positive effect of the magnetic nanocomposite increased by intercalation of long chains of hydrocarbons and building the organic–inorganic–magnetic nanohybrid structures because the intercalated hydrocarbons facilitated the dispersion of magnetic elements in the internal space of the nanolayered structures, causing homogeneous distribution inside the matrix of ZnO. This speculation was confirmed by observing clear absorbance for ZH-2-500, starting from 750 nm to 200 nm with two maxima at 650 nm and 350 nm, as shown in Fig. 11c. It means that the intercalation of magnetic nanoparticles inside the interlayered space of the nanohybrid led to good and order

dispersion inside the structure of zinc oxide after calcination, creating new optical active centers for ZnO.

This finding was confirmed by calculating their band gap energy. The band gap energy was determined by plotting the relation between $(\alpha h\nu)^2$ and energy $(h\nu)$, as shown in Fig. 12. The band gap energy E_g of ZAO was calculated by extending the straight line to the $(h\nu)$ axis to obtain the optical band gap energy at $(\alpha h\nu)^2$ of 0. It showed 3.15 eV, indicating a little shift from the band gap of pure ZnO because of the doping of aluminum inside the zinc oxide structure. In case of ZH-1-500, a little change was observed for the band gap energy because Fig. 12b shows 3.2 eV. On the other hand, the strong effect of the magnetic nanocomposite on the absorbance of ZH-2-500 was clear for narrowing the band gap energy to 2.75 eV, as shown in Fig. 12c. By comparing with pure zinc oxide, the narrowing was clearer because the reduction was from 3.3 eV to 2.75 eV, indicating that the organic–inorganic–magnetic nanohybrids has a strong positive effect on the optical properties of zinc oxide.

The weak and strong effect of magnetic elements on the band gap energy of ZnO, which is observed for the samples ZH-1-500 and ZH-2-500, respectively, agree with the XRD and SEM-EDX results. For ZH-1-500, the XRD results indicated that it has two mixed phasesone is the Al-doped ZnO and the other is cobalt iron oxide. SEM-EDX analysis (the new figure) showed that the percentages of Co and Fe inside the ZnO structure is zero. Therefore, the magnetic element has a weak effect on the Al-doped ZnO. For ZH-2-500, the XRD results showed only one phase ZnO and SEM-EDX analysis (the new figure) revealed the
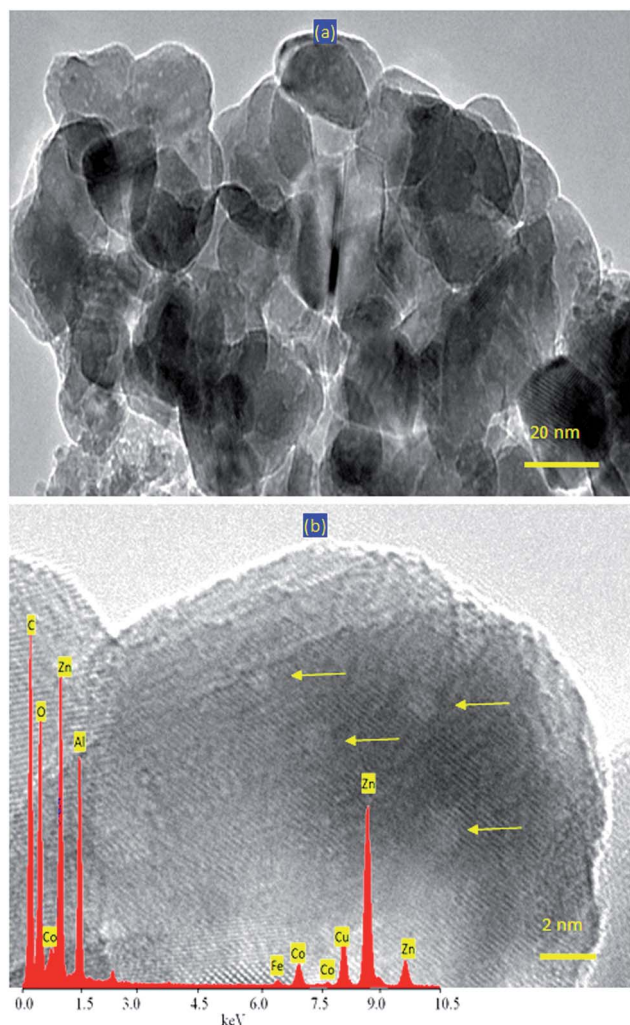
Fig. 9 TEM images of ZH-2-500: (a) 20 nm and (b) 2 nm (inset: EDX spectrum).

distribution of 2.01% Co and 1.38% Fe inside the ZnO structure, in addition to the presence of 10.96% Al. Therefore, the magnetic elements have a strong effect on the optical properties of ZnO.

Photocatalytic decomposition of naphthol green B dye

It is known that the improvement of the optical properties of the products of zinc oxides leads to positive effects on their photoactivities. In order to indicate these positive effects, the prepared products were used as photocatalysts for increasing the photocatalytic activity of zinc oxide to decompose and remove pollutants by light in a short time. In this way, the green colored dye naphthol green B was used as an example for colored pollutants. The photoactivities of zinc oxides (doped or non-doped) and their products based on magnetic nanocomposites and nanohybrids were studied through the photocatalytic degradation of naphthol green B. By irradiating the aqueous solution of naphthol green B with the UV light in the presence of the photocatalyst for a certain time, the absorbance of the liquid portion was measured. The reduction in the absorbance of the green dye at a wavelength of 715 nm showed the decomposition of the main skeleton of the dye. In addition, the decomposition of the naphthyl rings in the dye could be monitored from the absorbance peaks at 322 nm, 280 nm, and 230 nm, as shown in Fig. 13a and b.

The blank experiment, which was performed without the photocatalyst, indicated the high stability of naphthol green B for the irradiation of UV light. The photocatalytic decomposition of the green dye was examined as a function of the irradiation time of UV light in the presence of the photocatalyst, as seen in Fig. 13. When the aqueous solution of naphthol green B was mixed with the photocatalyst for 10 min in the dark, an appropriate change was observed, indicating that these photocatalysts have adsorption power. For reference, it was used as 0 min irradiation.

Fig. 13a showed the photocatalytic degradation of naphthol green B under UV light in the presence of ZH-1-500. By
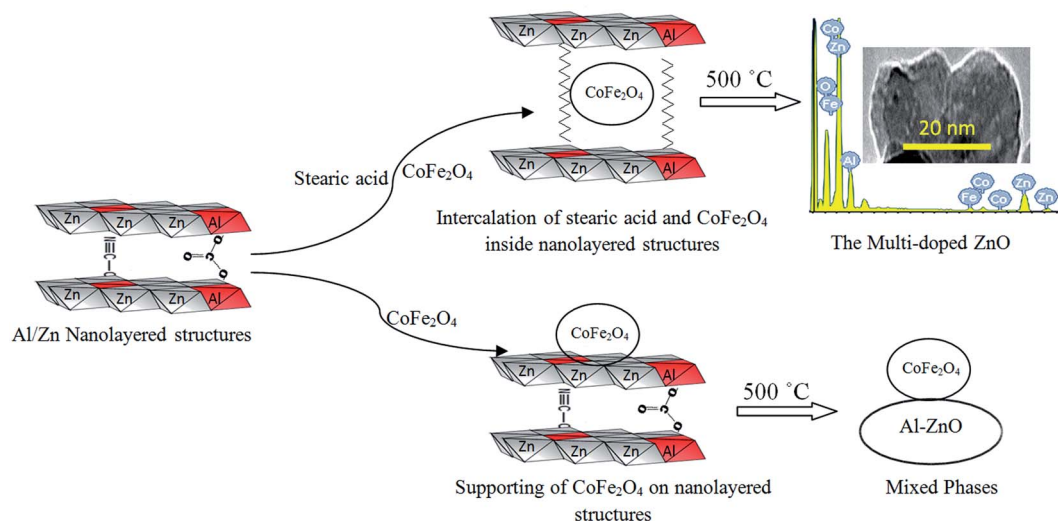

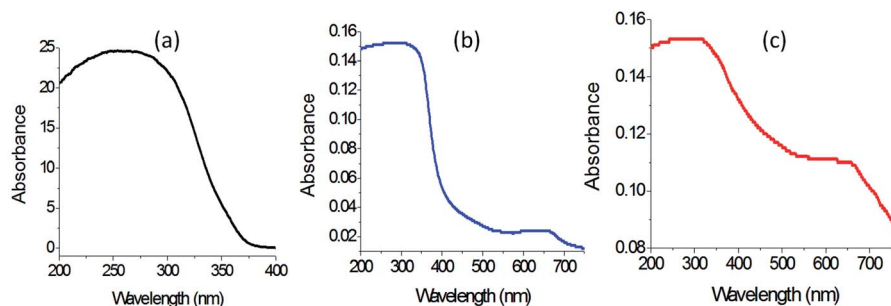**Fig. 10** Schematic representation of zinc oxide nanohybrids based on organic-inorganic-magnetic nanohybrids.

Fig. 11 UV-Vis absorbance of (a) ZAO-500, (b) ZH-1-500, and (c) ZH-2-500.
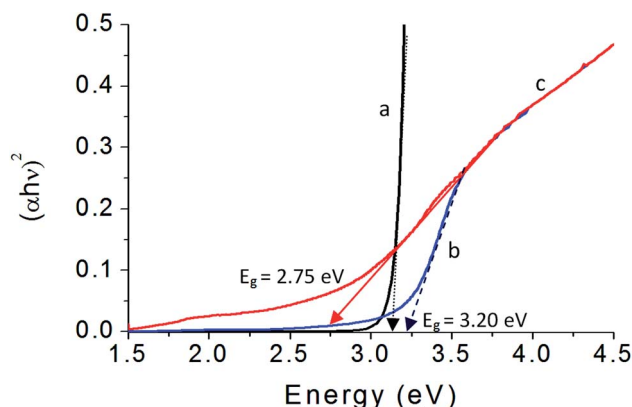

Fig. 12 Band gap energy of (a) ZAO-500, (b) ZH-1-500, and (c) ZH-2-500.

increasing the irradiation time, the photocatalytic degradation of naphthol green B increased. After 30 min of UV irradiation, a complete removal of the green color was observed, indicating high activity for ZH-1-500. Using ZH-2-500, the activity became higher, as shown in Fig. 13b. A complete photocatalytic degradation of naphthol green B was achieved after 15 min of UV irradiation. It means that ZH-2-500 is very active because it completely destroyed the green dye in a shorter time.

The high performance of the zinc oxide nanocomposite based on the nanohybrid ZH-2-500 was clear after comparison with ZAO-500, as shown in Fig. 14a, where the complete removal

of the green dye happened after 90 min of UV irradiation in the presence of ZAO-500. To confirm this finding, the photocatalytic degradation of naphthol green B was carried out in the presence of commercial and pure zinc oxide. The complete photocatalytic degradation of green dyes occurred after 51 min of UV-irradiation, confirming the high performance of the prepared multi-doped ZnO based on the sample ZH-2-500.

In order to indicate the effect of organic species on the optical activity, the kinetics of photocatalytic decolorization and degradation of naphthol green B were studied for both ZH-1-500 and ZH-2-500 by the following equation.

$$\ln([C_0]/[C]) = kt \tag{1}$$

The concentration of naphthol green B at different times is coded as $[C]$. The initial concentration of naphthol green B, which was expressed by the absorbance at time equal to zero, is coded as $[C_0]$. The rate reaction constant is k. The diagrams could be employed for kinetically determining the type of reactions by plotting the irradiation time in minutes against $\ln([C_0]/[C])$.

According to Fig. 14b, the diagrams showed straight lines, indicating pseudo-first-order reactions for the photocatalytic degradation and decolorization of naphthol green B using both ZH-1-500 and ZH-2-500.

Fig. 14b(1) showed that the rate reaction constant for the photocatalytic degradation of naphthol green B in the presence of ZH-1-500 is 0.089 min^{-1}. Using ZH-2-500, the reaction
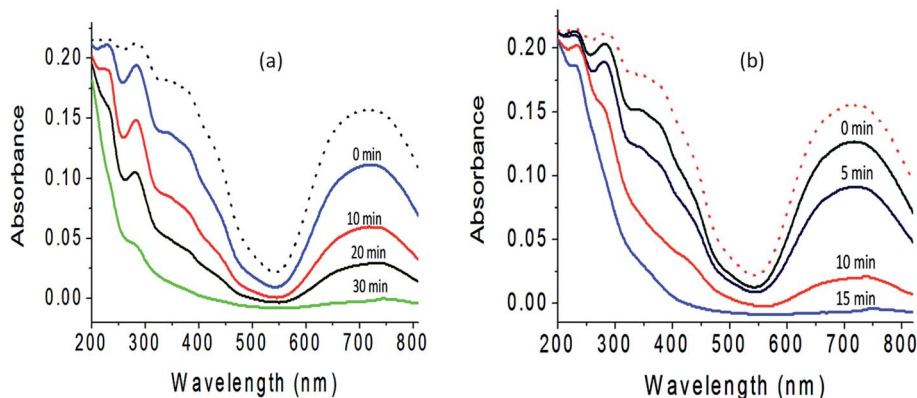

Fig. 13 Photocatalytic degradation of naphthol green B in the presence of (a) ZH-1-500 and (b) ZH-2-500.
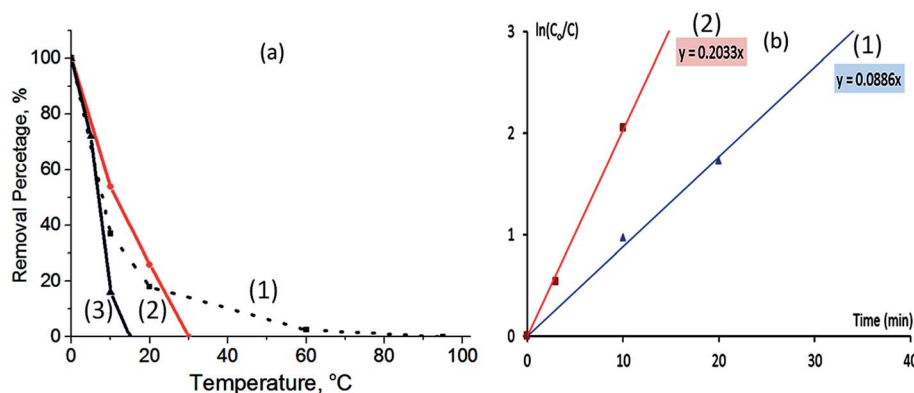
Fig. 14 (a) Removal percentage of the photocatalytic degradation of naphthol green B in the presence of (1) ZAO-500, (2) ZH-1-500, and (3) ZH-2-500, and (b) kinetics study of the photocatalytic degradation of naphthol green B in the presence of (1) ZH-1-500 and (2) ZH-2-500.

became faster because the rate reaction constant increased to 0.203 min^{-1}, as shown in Fig. 14b(2). The kinetics study concluded that the rate of photocatalytic degradation of naphthol green B in the presence of ZH-2-500 increased two times than that of ZH-1-500. The process of photocatalytic degradation of NH-2-500 was repeated two times with a fresh sample of the green dye to test the recyclability of the prepared photocatalysts. Similar results were observed, indicating the high recyclability of the produced photocatalysts. This conclusion showed the important role of organic species for the high performance of ZH-2-500.

Discussion

The fast photocatalytic degradation of the green dyes showed the excellent activity of the prepared zinc oxide nanohybrid ZH-2-500, which was produced from inorganic-magnetic-organic nanohybrids. The high performance of ZH-2-500 can be explained through the novel strategy for building the nanohybrid structure of ZH-2-500. The intercalation of the fine nanoparticles of the CoFe$_2$O$_4$ nanocomposite among the nanolayers of Al/Zn gave good chance of incorporation of this nanocomposite with zinc oxide structures during the crystallization process. Therefore, ZH-2-500 shows a highly crystalline structure of zinc oxide, and there are no peaks for aluminum or cobalt iron oxides. This good incorporation of the CoFe$_2$O$_4$ nanocomposite with the crystals of zinc oxide failed for the ZH-1-500 sample because the nanoparticles of the CoFe$_2$O$_4$ nanocomposite could not intercalate among the nanolayers of Al/Zn but were supported on the external surface of the Al/Zn plates. The good incorporation of the CoFe$_2$O$_4$ nanocomposite with the crystals of zinc oxide doped with aluminum created new optically-active centers inside zinc oxide nanohybrid ZH-2-500 and caused a reduction of its band gap energy, thus making it very active, because of the low band gap energy of CoFe$_2$O$_4$ (1.32 eV).[48] At the same time, some sites of Zn in zinc oxide were occupied by CoFe$_2$O$_4$ atoms, producing new optically-active centers called shallow traps between the valence band and the conduction band, leading to a decrease in the band gap energy.[3,49]

This low band gap energy and the small size of the nanoparticles of the zinc oxide nanohybrid ZH-2-500 have a strong effect on the mechanism of photocatalytic degradation of the green dyes. The mechanism of photocatalytic degradation in sunlight depends on two important stages.[50–52] The first stage is the production of a strong oxidizing agent as follows.

(a) By UV light, the surface of the photocatalyst was excited through the absorption of enough energy for transferring electrons from the valence band to the conduction band, thus creating holes in the former.

$$h\nu + ZH \rightarrow h^+ \text{ (valence band)} + e^- \text{ (conduction band)} \quad (2)$$
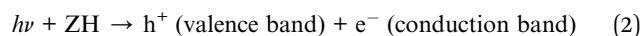
(b) In the same time, oxygen molecules were physically adsorbed on the surface of the photocatalyst ZH, which captured the electron from the conduction band, thus producing ions.
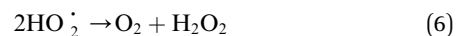
$$(O_2)_{ads} + e^- \rightarrow O_2^{\cdot-} \quad (3)$$

(c) The holes in the valence band neutralized the hydroxyl groups, which were produced from water molecules, thus producing hydroxyl radicals.
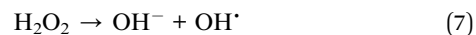
$$(H_2O \leftrightarrow H^+ + OH^-) + h^+ \rightarrow OH^\cdot + H^+ \quad (4)$$
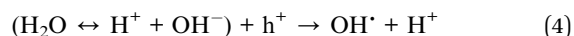
(d) Neutralization of $O_2^{\cdot-}$

$$O_2^- + H^+ \rightarrow HO_2^\cdot \quad (5)$$

(e) Production of hydrogen peroxide

$$2HO_2^\cdot \rightarrow O_2 + H_2O_2 \quad (6)$$

(f) Hydrolysis of hydrogen peroxide

$$H_2O_2 \rightarrow OH^- + OH^\cdot \quad (7)$$
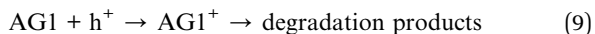
The hydroxyl free radicals ($^\cdot$OH) and superoxide radical anion ($^\cdot O_2^-$) are strong oxidizing agents. The second stage

focuses on the oxidation reactions of the pollutants by different kinds of oxidizing agents.

$$\text{(g)} \quad AG1 + {}^{\cdot}O_2{}^- \rightarrow \text{degradation compounds} + CO_2 + H_2O \quad (8)$$
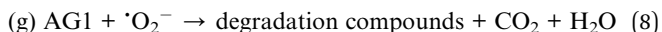
(h) Also, the holes started the degradation process of the pollutants.

$$AG1 + h^+ \rightarrow AG1^+ \rightarrow \text{degradation products} \quad (9)$$

The band gap of ZH-2-500 is not very small to accelerate the recombination reactions, in addition to the shallow traps that help in separating the electrons and holes. Therefore, the degradation reaction continues as shown in eqn (5) and (6). In this way, the colored pollutants disappeared after 15 min of UV-light irradiation.

Experimental

Heterostructured hybrids such as inorganic–magnetic and organic–inorganic–magnetic systems are good candidates for creating unusual optical properties for zinc oxide, which cannot be achieved by conventional methods.
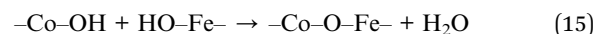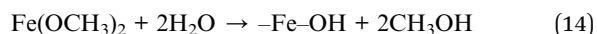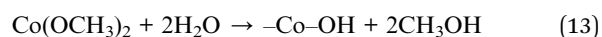
In order to build organic–inorganic–magnetic nanohybrids based on zinc oxide, three types of nanomaterials were prepared. The first type was very fine nanoparticles of cobalt iron oxides nanocomposite, which were used as a filler for the nanohybrids. The second one was nanolayered structures based on Al/Zn LDHs. The third type depended on the long chains of organic fatty acid to expand and widen the interlayer spacing of the nanolayered structures, as shown in Fig. 15. This widening and expansion can facilitate the insertion of magnetic nanoparticles among the nanolayers of Al/Zn LDHs. To study the important role of organic fatty acids, an inorganic–magnetic nanohybrid was prepared without organic species.

Preparation of nanoparticles of magnetic nanocomposites

A solvothermal technique was used for preparing very fine nanoparticles of cobalt iron nanocomposite. Cobalt(II) acetate (0.096 M) and iron(II) acetate (0.096 M) were reacted with 350 mL of methanol at room temperature for 5 h to produce a sol of methoxides, as shown in the following equations.

$$CH_3OH + Co(OCOCH_3)_2 \rightarrow 2CH_3COOH + Co(OCH_3)_2 \quad (10)$$

$$CH_3OH + Fe(OCOCH_3)_2 \rightarrow 2CH_3COOH + Fe(OCH_3)_2 \quad (11)$$

A similar amount of ethanol was added to the mixture. To complete the reaction under supercritical conditions of pressure and temperature, the mixture was placed inside an autoclave. The mixture was heated at a slow rate of $1 °C \ min^{-1}$ to reach 260 °C under a high pressure of 75 bar. The sol was converted to a gel by the polycondensation or polyesterification reactions that result in a dramatic increase in the viscosity of the solution during heating inside the autoclave. Polycondensation reactions continue until the gel is transformed into a solid mass of $CoFe_2O_4$

$$C_2H_5OH + CH_3COOH \rightarrow CH_3COOC_2H_5 + H_2O \quad (12)$$

$$Co(OCH_3)_2 + 2H_2O \rightarrow -Co-OH + 2CH_3OH \quad (13)$$

$$Fe(OCH_3)_2 + 2H_2O \rightarrow -Fe-OH + 2CH_3OH \quad (14)$$

$$-Co-OH + HO-Fe- \rightarrow -Co-O-Fe- + H_2O \quad (15)$$

At the final stage, the pressure was slowly released under the flow of nitrogen to avoid oxidation reactions. The solvents were removed. At the same time, the temperature of the autoclave decreased to room temperature. The fine powder of the product was easily collected.

Preparation of nanolayered structures and nanohybrids

Three samples were prepared for designing nanolayered structure, inorganic–magnetic nanohybrid, and organic–inorganic–magnetic nanohybrid. The nanolayered structure of Al/Zn LDH was prepared by mixing aqueous solutions (0.069 mol) of aluminum nitrate with zinc nitrate in the presence of 0.5 mol of urea. The molar ratio of aluminum to zinc was 1 : 3. By keeping the temperature of the mixture at 80 °C, the nanolayers of LDH were precipitated during the hydrolysis of urea because the nature of the reaction medium gradually changed from acidic to alkaline. A white precipitate was obtained after 12 h of reaction. It was filtered and washed by distilled water. By drying at room temperature, the product was collected and coded as ZAO.

The inorganic–magnetic nanohybrid was prepared by the same procedure, noting that the nanolayers of Al/Zn LDH were precipitated in the presence of 0.5 g of the prepared nanoparticles of the cobalt iron oxides nanocomposite. The product was collected and coded as ZH-1.
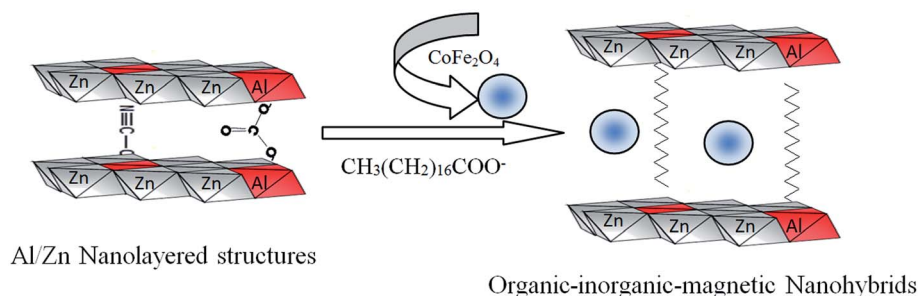

Fig. 15 Schematic representation of building organic–inorganic–magnetic nanohybrids.

The organic–inorganic–magnetic nanohybrid was synthesized by adding 100 mL of the aqueous solution of 5% stearic acid sodium salt while preparing the Al/Zn nanolayered structure. Also, 0.5 g of the prepared nanoparticles of the cobalt iron oxide nanocomposite was mixed with the aqueous solution (0.069 mol) of aluminum nitrate with zinc nitrate in the presence of 0.5 mol of urea. By keeping the temperature of the mixture at 80 °C, the product was obtained after 12 h of the reaction. After filtration and washing, the product was dried under vacuum at room temperature. The sample was coded as ZH-2.

Preparation of nanohybrids and nanocomposite based on oxides

The nanolayered structure of Al/Zn LDH was thermally treated at 500 °C to produce the nanocomposite of zinc and aluminum oxides. It was represented by ZAO-500. By calcination at 500 °C, the nanohybrid ZH-1 was converted the stable nanohybrid composed of magnetic and non-magnetic oxides. It was represented by ZH-1-500. The organic–inorganic–magnetic nanohybrid ZH-2 was transformed to a new structure of the nanohybrid through thermal treatment at 500 °C. It was represented by ZH-2-500.

Physical measurements

Nanolayered structures and crystalline structures of the prepared samples were identified by a Bruker-AXS system (Bruker Company, Karlsruhe, Germany) with Cu-Kα radiation for X-ray diffraction analysis (XRD). An electron probe microanalyzer JED 2300 (JEOL Company, Tokyo, Japan) was used for detecting the elements in the prepared samples through energy dispersive X-ray spectroscopy (EDX). For studying the thermal behavior of the prepared samples, thermogravimetric analyzer TA series Q500 and differential scanning calorimeter (DSC) TA series Q600 (TA company, New Castle, PA, USA) were used under the flow of nitrogen. For imaging the nanosize and morphology of the prepared materials, a transmission electron microscope (TEM) JEM 2100F (JEOL Company, Tokyo, Japan) was used with different magnifications. The optical properties were measured for the prepared samples through the diffuse reflectance technique. A UV/VIS/NIR Shimadzu 3600 spectrophotometer (Shimadzu, Columbia, MD, USA) was used for measuring the absorbance of the liquid and solid samples.

Photocatalytic activity

Photocatalytic degradation of aqueous solutions of industrial dyes was carried out for measuring the photocatalytic activity of the prepared materials for the purification of water. Photocatalytic reactions were carried out inside a quartz immersion well reactor RQ400, which was supplied by Photochemical Reactors Limited company in Camberley Surrey, UK. The photocatalytic reactions were accomplished inside a 400 mL standard reaction flask Model 3308, which was made of quartz glass. A 400-watt power supply 3140/PX0783 was used with a 400 W medium pressure mercury lamp 3040/PX0686. In the current study, an aqueous solution of Naphthol green B, which was

used as a pollutant, was prepared with a low concentration of 4×10^{-4} M. According to the Beer–Lambert law, when the initial concentration of the dye was low, the intensity of the measured spectrum of the dye can be used to express the dye concentration. Thus, the changes in the concentrations of naphthol green B were monitored by measuring the absorbance at 714 nm, which considered the characteristic band of naphthol green B. Using a photocatalytic reactor, the green solution was mixed with one of the prepared materials and irradiated by UV light at room temperature. To maintain the temperature of the photocatalytic reaction, the glass reactor was equipped with a cooling system. Before irradiation of UV light and after stirring the mixture for 5 min in the dark, the concentration of the green mixture was measured for detecting the adsorption of the dye on the catalyst. At different intervals of irradiation time, a fixed amount of the solution was extracted and measured by a UV-Vis spectrophotometer to determine the concentration of the remaining dye in the solution.

Conclusions

In the present study, dual aims were achieved for designing the multi-doped zinc oxide for the useful and effective of purifying water with UV light. This aim focused on a new strategy for building inorganic–magnetic–organic nanohybrids as a source for producing the Co–Fe–Al-doped zinc oxide. In this context, nanoparticles of $CoFe_2O_4$ with size less than 5 nm were prepared and used as seeds for building nanohybrids. The inorganic–magnetic–organic nanohybrid was formed through intercalation reactions with long chains of hydrocarbons of stearic acid in the presence of the prepared $CoFe_2O_4$ nanoparticles. The XRD results suggested the formation of nanohybrids through the expansion of the interlayered spacing of the nanolayered structure from 0.755 nm to 2.02 nm. FIIR and thermal analyses confirmed the nanohybrid formation. The magnetic–inorganic nanohybrid was prepared without organic species for comparison. The characterization techniques showed that the prepared inorganic–magnetic–organic nanohybrid was useful for producing multi-doped zinc oxide by thermal treatment. XRD results, TEM images, and SEM-EDX analysis confirmed the formation of zinc oxide doped with aluminum, cobalt, and iron. By measuring the optical properties, a clear reduction in the band gap energy was observed for the multi-doped zinc oxide compared with the Al-doped and undoped zinc oxide. This reduction in the band gap energy from 3.20 eV to 2.75 eV led to the high activity of the multi-doped zinc oxide in UV light.

This high activity was proven by the complete removal of naphthol green B after 15 min of UV light irradiation in the presence of multi-doped zinc oxide. These results were confirmed by comparison with the Al-doped zinc oxide, which indicated that the pure and Al-doped zinc oxide removed the green dyes after 90 min of light irradiation. Also, the kinetic study showed that the multi-doped zinc oxide, which is based on an inorganic–magnetic–organic nanohybrid, is better than the zinc oxide produced from an inorganic–magnetic nanohybrid. Finally, it can be concluded that this strategy for

designing a photoactive nanohybrid can lead to positive tools for overcoming environment- and water-related problems using the fast technique for purifying water.

Conflicts of interest

There are no conflicts to declare.

Acknowledgements

References

1 M. Al-Yaari, T. A. Saleh and O. Saber, *RSC Adv.*, 2021, **11**, 380.

2 O. Saber, A. Abdullah, A. Adil and A. Osama, *RSC Adv.*, 2019, **9**, 30509.

3 O. Saber, H. M. Kotb, M. Osama and H. A. Khater, *Nanomaterials*, 2022, **12**, 440.

4 O. Saber, N. M. Shaalan, F. Ahmed, S. Kumar and A. Alshoaibi, *Crystals*, 2021, **11**, 1268.

5 A. Alshoaibi, O. Saber and F. Ahmed, *Crystals*, 2021, **11**, 550.

6 O. Saber, A. Alshoaibi, M. Al-Yaari and M. Osama, *Molecules*, 2020, **25**, 4484.

7 O. Saber and H. M. Kotb, *Appl. Sci.*, 2020, **10**, 1786.

8 O. Saber, A. Aljaafari, M. Osama and H. Alabdulgader, *ChemistryOpen*, 2018, **7**, 833–841.

9 O. Saber, H. Alomair, M. Abu-Abdeen and A. Aljaafari, *Acta Metall. Sin. (Engl. Lett.)*, 2018, **31**, 533–546.

10 S. Sharma, V. Dutta, P. Raizada, A. Hosseini-Bandegharaei, P. Singh and V.-H. Nguyen, *Environ. Chem. Lett.*, 2021, **19**, 271–306.

11 S. Sharma, V. Dutta, P. Raizada, V. K. Thakur, A. K. Saini, D. Mittal, V.-H. Nguyen, T. Ahamad, C. C. Nguyen, S. Y. Kim, Q. V. Le and P. Singh, *Mater. Lett.*, 2022, **313**, 131716.

12 A. Fujishima and K. Honda, *Nature*, 1972, **238**, 37–38.

13 M. S. Gui and W. D. Zhang, *Nanotechnology*, 2011, **22**, 265601.

14 X. B. Chen, L. Liu, P. Y. Yu and S. S. Mao, *Science*, 2011, **331**, 746–750.

15 M. C. Yeber, J. Roderiguez, J. Freer, J. Baeza, N. Duran and H. D. Mansilla, *Chemosphere*, 1999, **39**, 1679–1688.

16 M. A. Behnajady, N. Modirshahla and R. Hamzavi, *J. Hazard. Mater. B*, 2006, **133**, 226–232.

17 J. H. Sun, S. Y. Dong, Y. K. Wang and S. P. Sun, *J. Hazard. Mater.*, 2009, **172**, 1520–1526.

18 Q. Wang, C. Tang, C. Jiang, D. Du, F. Wang and J. Song, *Acta Metall. Sin. Engl. Lett.*, 2016, **29**, 237–242.

19 W. Zhou, X. Li, L. Qin and S. Kang, *J. Mater. Sci. Technol.*, 2017, **33**, 47–51.

20 S. Patial, P. Raizada, V. Hasija, P. Singh, V. Kumar Thakur and V.-H. Nguyen, *Mater. Today Energy*, 2021, **19**, 100589.

21 N. Alhokbany, T. Ahamad and S. M. Alshehri, *J. Environ. Chem. Eng.*, 2022, **10**, 107681.

22 V. Hasija, P. Raizada, A. Sudhaik, P. Singh, V. K. Thakur and A. A. P. Khan, *Solid State Sci.*, 2020, **100**, 106095.

23 K. Perumal, S. Shanavas, T. Ahamad, A. Karthigeyan and P. Murugakoothan, *J. Environ. Sci.*, 2023, **125**, 47–60.

24 M. Shekofteh-Gohari, A. Habibi-Yangjeh, M. Abitorabi and A. Rouhi, *Crit. Rev. Environ. Sci. Technol.*, 2018, **48**, 806–857.

25 C. Liu, H. Xu, L. Wang and X. Qin, *Acta Metall. Sin. Engl. Lett.*, 2017, **30**, 36–44.

26 X. Bai, L. Wang, R. Zong, Y. Lv, Y. Sun and Y. Zhu, *Langmuir*, 2013, **29**, 3097–3105.

27 Y. Leung, X. Chen, A. Ng, M. Guo, F. Liu, A. Djurisic, W. Chan, X. Shi and M. Van Hove, *Appl. Surf. Sci.*, 2013, **271**, 202–209.

28 J. Wojnarowicz, T. Chudoba, I. Koltsov, S. Gierlotka, S. Dworakowska and W. Lojkowski, *Nanotechnology*, 2019, **29**, 06561.

29 A. Pimentel, S. H. Ferreira, D. Nunes, T. Calmeiro, R. Martins and E. Fortunato, *Materials*, 2016, **9**, 299.

30 P. Samadipakchin, H. R. Mortaheb and A. Zolfaghari, *J. Photochem. Photobiol. A Chem.*, 2017, **337**, 91.

31 Y. Zhang, M. K. Ram, E. K. Stefanakos and Y. D. Goswami, *J. Nanomater.*, 2012, **12**, 624520.

32 L. J. Diguna, A. D. Fitriani, B. R. Liasari, G. E. Timuda, W. B. Widayatno, A. S. Wismogroho, S. Zeng, M. D. Birowosuto and M. I. Amal, *Crystals*, 2021, **11**, 6.

33 H. Chen, L. Zhao, X. He, G. Wang, X. Wang, W. Fang and X. Du, *Acta Metall. Sin. Engl. Lett.*, 2017, **30**, 104–112.

34 J. B. Zhong, J. Z. Li, X. Y. He, J. Zeng, Y. Lu, W. Hu and K. Lin, *Curr. Appl. Phys.*, 2012, **12**, 998–1001.

35 J. Sin, S. Lam, K. Lee and A. Mohamed, *Ceram. Int.*, 2013, **39**, 5833–5843.

36 M. Ahmad, E. Ahmed, Y. Zhang, N. R. Khalid, J. Xu, M. Ullah and Z. Hong, *Curr. Appl. Phys.*, 2013, **13**, 697–704.

37 L. Huang, N. Ren, B. Li and M. Zhou, *Acta Metall. Sin. Engl. Lett.*, 2015, **28**, 281–288.

38 M. H. Haja sheriff, S. Murugan, A. Manivasaham and R. Ashok Kumar, *Mater. Today Proc.*, 2021, **47**, 1717–1723.

39 A. Riaz, A. Ashraf, H. Taimoor, S. Javed, M. A. Akram, M. Islam, M. Mujahid, I. Ahmad and K. Saeed, *Coatings*, 2019, **9**, 202.

40 A. B. Lavand and Y. S. Malghe, *J. Asian Ceram. Soc.*, 2018, **3**, 305–310.

41 S. Hamrouni, M. S. AlKhalifah, M. S. El-Bana, S. K. Zobaidi and S. Belgacem, *Appl. Phys. A*, 2018, **124**, 555.

42 A. A.-G. Farrag and M. R. Balboul, *J. Sol-Gel Sci. Technol.*, 2016, **82**, 269–279.

43 X. Yan, S. Venkataraj and A. G. Aberle, *Int. J. Photoenergy*, 2015, **2015**, 1–10.

44 M. R. Islam, M. Rahman, S. F. U. Farhad and J. Podder, *Surf. Interfaces*, 2019, **16**, 120–126.

45 R. Mahdavi and S. S. A. Talesh, *Adv. Powder Technol.*, 2017, **28**, 1418–1425.

46 C. Aydın, M. S. AbdEl-sadek, K. Zheng, I. S. Yahia and F. Yakuphanoglu, *Opt. Laser Technol.*, 2013, **48**, 447–452.

47 K. Ravichandran, E. Sindhuja, R. Uma and T. Arun, *Surf. Eng.*, 2017, **33**, 512–520.

48 J. Parhizkar and M. H. Habibi, *J. Water Environ. Nanotechnol.*, 2019, **4**, 17–30.

49 A. P. Singh, S. Kumari, R. Shrivastav, S. Dass and V. R. Satsangi, *Int. J. Hydrog. Energy*, 2008, **33**, 5363–5368.

50 M. T. S. Chani, S. B. Khan, M. M. Rahman, T. Kamal and A. M. Asiri, *Science*, 2022, **34**, 101841.

51 F. Azeez, E. Al-Hetlani, M. Arafa, Y. Abdelmonem, A. A. Nazeer, M. O. Amin and M. Madkour, *Sci. Rep.*, 2018, **8**, 7104.

52 M. Chadwick, J. Goodwin, E. Lawson, P. Mills and B. Vincent, *Colloids Surf., A*, 2002, **203**, 229–236.